PERGAMON

International Journal of Heat and Mass Transfer 42 (1999) 1801–1811

International Journal of
HEAT and MASS
TRANSFER

Natural convection from a horizontal cylinder in a rectangular cavity

G. Cesini[a], M. Paroncini[a], G. Cortella[b,*], M. Manzan[b]

[a] *Dipartimento di Energetica, Università degli Studi di Ancona, via delle Brecce Bianche, I 60100 Ancona, Italy*
[b] *Dipartimento di Energetica e Macchine, Università degli Studi di Udine, via delle Scienze 208, I 33100 Udine, Italy*

Received 24 October 1997; in final form 10 August 1998

Abstract

A numerical and experimental analysis is performed for natural convection heat transfer from a horizontal cylinder enclosed in a rectangular cavity. The temperature distribution in the air and the heat transfer coefficients are measured by a holographic interferometer and compared with numerical predictions obtained by a finite-element procedure based on the streamfunction-vorticity formulation of the momentum equations. The influence of the Rayleigh number and the geometry of the cavity on the heat transfer are investigated. © 1998 Elsevier Science Ltd. All rights reserved.

Key words: Natural convection; Interferometry; Confined motion

Nomenclature

a	thermal diffusivity
D	diameter of the cylinder
g	modulus of the gravity vector
h	overall heat transfer coefficient on the upper wall
H	height of the cavity
L	length of the cavity
$\boldsymbol{n}$	normal to the boundary surface
Nu	local Nusselt number
$\overline{Nu}$	average Nusselt number
r	radius of the cylinder
Ra	Rayleigh number
s	area of the cylinder surface
$\mathbf{s}$	boundary tangent vector
t	temperature
u	velocity component
w	velocity component
W	width of the cavity
W^*	aspect ratio of the cavity
x	Cartesian co-ordinate
z	Cartesian co-ordinate.

Greek symbols

α	angle (counterclockwise from the bottom of the cylinder)
β	coefficient of thermal expansion
ΔT	temperature difference ($t_c - t_w$)
ϑ	time
ν	kinematic viscosity
ψ	streamfunction
ω	vorticity.

Subscripts

a	ambient
c	cylinder
s	tangential component
w	wall.

1. Introduction

Heat transfer by natural convection from a horizontal cylinder in cavities has various applications, ranging from heat exchangers to solar heating and to cooling of electronic packages. Natural convection from a single horizontal cylinder [1] and from horizontal tube arrays [2] has been investigated in the past. Natural convection heat transfer in rectangular cavities heated from below [3, 4]

---

* Corresponding author. Tel.: 0039 0432 558022; fax: 0039 0432 558027; e-mail: giovanni.cortella@uniud.it

0017-9310/98/$ - see front matter © 1998 Elsevier Science Ltd. All rights reserved
PII: S0017-9310(98)00266-X

and heated from one side [5–7] has been widely investigated also. However, comparatively little information is available for natural convection from horizontal cylinders enclosed in a cavity.

In this paper, a numerical and experimental analysis is performed for natural convection from a single horizontal heated cylinder enclosed in a cavity of rectangular cross section in which vertical side walls are isothermal, while the lower horizontal and the end walls are adiabatic. At the upper horizontal wall, conductive heat transfer through the wall is imposed, for a better reproduction of the experimental set-up. Due to the depth of the experimental apparatus, the influence of the end walls can be neglected in the central cross section, where the resulting velocity and thermal fields are two-dimensional; therefore, the numerical analysis reported here is based on a two-dimensional finite-element discretization for incompressible laminar flows. In the framework of the streamfunction-vorticity formulation, a fully segregated approach is followed, in which the governing differential equations are completely uncoupled and solved in sequence. The method employed has been previously successfully utilised for solving higher Rayleigh number problems than encountered here [6].

The temperature distribution is experimentally measured both by real-time and double-exposure holographic interferometry. The real-time technique is used in order to reveal the presence of plume oscillations, while the double-exposure technique is used for steady-state measurements. Holographic interferometry shows the typical advantages over the classical optical techniques, such as high precision and sensitivity, very low noise level, and the possibility of displaying the temperature distribution across the whole investigated region.

The objective of the heat transfer analysis is the investigation of the Nusselt number distribution around the cylinder at different aspect ratios of the cavity and at various Rayleigh numbers. Comparisons between numerical and experimental results are performed on three cavities whose height is $H = 57$ mm and widths are $W = 30$, 40 and 50 mm, containing a cylinder having a diameter, $D = 14$ mm. Therefore, the H/D ratio is 4.07. Since the aspect ratio W^* of the cavity is defined as

$$W^* = \frac{W}{D} \tag{1}$$

the aspect ratios investigated for the comparisons are $W^* = 2.1$, 2.9 and 3.6, respectively. The comparisons concern the Rayleigh numbers $Ra = 1.3 \times 10^3$, 2.4×10^3 and 3.4×10^3, the Rayleigh number being defined as

$$Ra = \frac{g\beta(t_c - t_w)D^3}{\nu a}. \tag{2}$$

The experimental fluid is air, whose physical properties in equation (2) are estimated at the average temperature between the cylinder and the wall temperature.

Further calculations are performed in a wider range of operating conditions, i.e. at $W^* = 2.1$, 2.9, 3.6 and 4.3, and at Rayleigh numbers from 1.3×10^3 up to 7.5×10^4.

The three computational domains utilised are represented in Fig. 1, together with the boundary conditions. The computational domains do not take into account the symmetry of the problem, because when the Rayleigh number is high, both non-stationary and asymmetric solutions can be obtained. However, the results reported here concern only stationary situations, in which the iterative calculation process is concluded when the difference in the Euclidean norm for temperatures between two consecutive steps is lower than 10^{-5}.

2. Governing equations and numerical method

Using the Boussinesq approximation for two-dimensional incompressible laminar flow, the streamfunction–vorticity equations can be written as

$$\frac{\partial^2\psi}{\partial x^2} + \frac{\partial^2\psi}{\partial z^2} = -\omega \tag{3}$$

and

$$\frac{\partial\omega}{\partial\vartheta} + u\frac{\partial\omega}{\partial x} + w\frac{\partial\omega}{\partial z} = \nu\left(\frac{\partial^2\omega}{\partial x^2} + \frac{\partial^2\omega}{\partial z^2}\right) + g\beta\frac{\partial t}{\partial x} \tag{4}$$

respectively. In equations (3) and (4) ψ is the streamfunction, ω is the vorticity, ϑ is the time, t is the temperature ν is the kinematic viscosity, β is the coefficient of thermal expansion, x and z are Cartesian co-ordinates defined in such a way that the x-axis is horizontal and the z-axis is vertical, opposite to the gravity vector. The x- and z-axis velocity components are

$$u = \frac{\partial\psi}{\partial z} \tag{5}$$

$$w = -\frac{\partial\psi}{\partial x} \tag{6}$$

respectively, while

$$\omega = \frac{\partial w}{\partial x} - \frac{\partial u}{\partial z} \tag{7}$$

is the vorticity.

The energy equation can be written as

$$\frac{\partial t}{\partial\vartheta} + u\frac{\partial t}{\partial x} + w\frac{\partial t}{\partial z} = a\left(\frac{\partial^2 t}{\partial x^2} + \frac{\partial^2 t}{\partial z^2}\right) \tag{8}$$

for a fluid with constant properties, when volumetric

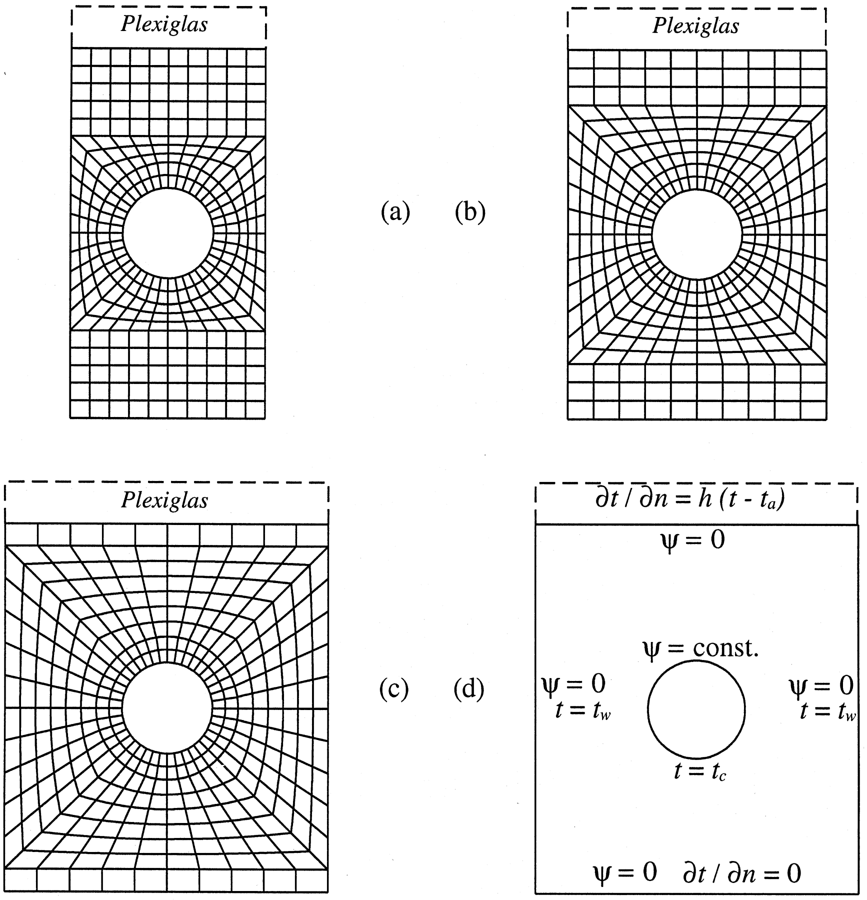

Fig. 1. Computational domain: (a) $W^* = 2.1$, (b) $W^* = 2.9$ and (c) $W^* = 3.6$; (d) boundary conditions.

heating is absent and the effects of viscous dissipation can be neglected.

As shown in Fig. 1(d), at the two isothermal cavity walls and at the cylinder surface we have $t = t_w$ and $t = t_c$, respectively, while the lower horizontal wall is assumed to be adiabatic. On the contrary, as already pointed out, adiabatic conditions are not imposed directly at the upper horizontal wall. In fact, in the experimental apparatus the smaller thickness of this wall does not guarantee adiabatic boundary conditions and therefore, for a more precise simulation, the computational domain takes into account the heat flux from the cavity to the ambient, through the solid layer of Plexiglas whose thermal properties are known. The overall heat transfer coefficient is estimated to be $h = 10$ W m^{-2} K^{-1}. At the walls of the cavity the value of the streamfunction is specified, while, at the internal boundary represented by the cylinder, the streamfunction is constant but has an unknown value which must be determined as part of the solution process [8]. At the cavity and cylinder boundaries also the normal derivatives of the streamfunction are specified as

$$u_s = -\frac{\partial \psi}{\partial n} = 0 \tag{9}$$

where u_s is the velocity component in the direction of the counter-clockwise oriented tangent vector **s**. However, this additional information cannot be used for the solution of the streamfunction equation, because it would overspecify the problem. Consequently, the information on the normal derivative of the streamfunction must be incorporated in the boundary condition for the vorticity. Therefore, the values of the wall vorticity are obtained by solving a discretised version of equation (3), where the boundary condition (9) is taken into account [9].

The local Nusselt number, at any point of the cylinder surface, is estimated as

$$Nu = \left(\frac{\partial t}{\partial r}\right)_{r=D/2} \frac{D}{\Delta t} \tag{10}$$

where the temperature gradient is computed from the nodal heat flow rates. According to equation (10), an average value of the Nusselt number on the cylinder surface can be defined as

$$\overline{Nu} = \frac{1}{\pi D}\int_0^{\pi D} Nu \, ds. \tag{11}$$

3. Experimental apparatus

The main components of the experimental apparatus, represented in Fig. 2, include the test-cell, filled with air at atmospheric pressure, the holographic interferometer and the data acquisition system.

A schematic drawing of the test cell is shown in Fig. 3. The height H is 57 mm, while the width W can be changed from 30 to 50 mm so that the aspect ratio $W^* = W/D$ ranges between 2.1 and 3.6.

The lateral vertical walls are made of aluminium and are cooled by circulating a heat transfer fluid through a metal jacket attached to the back surface. The top and bottom surfaces of the enclosure are made of Plexiglas, while the end vertical walls are made of glass in order to allow optical access to the cavity. The dimension, $L = 0.42$ m, of the test cell in the direction parallel to the laser beam is large enough to allow neglecting end-effects. Therefore the air enclosure may be considered as a two-dimensional rectangular cavity.

The cylinder is made of aluminium with a polished external surface, and it is positioned at the centre of the cavity. The finished outer diameter is $D = 14$ mm and its length is $L = 0.42$ m, which corresponds to 30 times the diameter D. The relatively thick wall of the cylinder (1 mm) aids the attainment of the desired uniform surface temperature. The cylinder surface temperature t_c, is higher than the wall temperature t_w, and it is maintained by circulating a fluid inside the cylinder.

The light source is an argon-ion laser with a nominal power rating of 4 W, with etalon for the 514.5 nm wave length. Both object and reference beams have a maximum

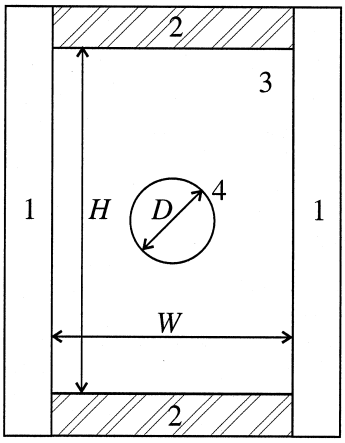

Fig. 3. Schematic drawing of the test cell: (1) walls at surface temperature t_w; (2) Plexiglas layers; (3) air; (4) cylinder at surface temperature t_c.

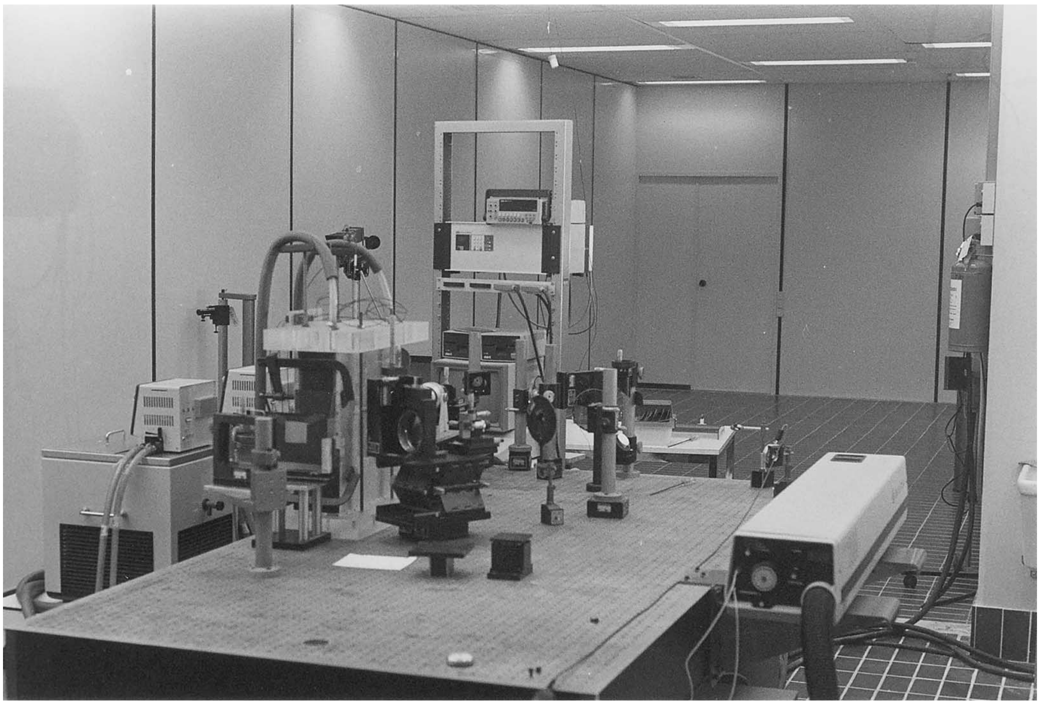

Fig. 2. Experimental apparatus.

diameter of 0.15 m. The optical set-up allows the use of double-exposure or real-time holographic interferometry techniques, for steady-state and temporal evolution measurements of heat transfer processes respectively [10]. The real-time technique has been used also to check the presence of plume oscillations. A copper–constantan thermocouple is located in the core of the air region to provide a reference temperature for the evaluation of the interferograms. The temperature of the cylinder and of the walls, measured by other thermocouples, cannot be used as reference, since their exact position in the interferograms is uncertain due to diffraction effects. The holograms have been obtained with the interferometer infinite fringe position field, so that the fringe pattern shows directly the distribution of the isothermal lines. The interferograms are evaluated by using a travelling microscope to obtain the intensity distribution. Density and temperature distribution are obtained by the usual methods of inversion [11]. According to Hauf and Grigull [11], the expected accuracy for small fringe numbers (less than 30) can be of about 10%.

4. Results

For a horizontal heated cylinder in natural convection, the Nusselt number is a function of the Rayleigh number only. When the geometry is modified to include confining walls, the Nusselt number becomes a function of the geometry as well. The experimental work in the present paper concerns a horizontal uniformly heated cylinder located at the centre of the cavity. The Rayleigh number, as previously defined, ranges between 1.3×10^3 and 3.4×10^3, with aspect ratios W^* equal to 2.1, 2.9 and 3.6.

Comparisons are made between numerical and experimental results: in Figs 4–6 the stream-lines and temperature distributions calculated with the numerical method are reported, as a function of the aspect ratio W^* and of the Rayleigh number.

Two recirculation zones are clearly shown beside the cylinder, growing in intensity with increasing Rayleigh numbers. The temperature distribution on the upper part of the cavity is characteristic of natural convection from circular objects.

The fluid motion is strongly dependent on the aspect ratio of the cavity. In fact, taking as reference Fig. 4, in which the results for the lowest W^* investigated are reported, the recirculation is confined to the upper part of the cavity, while the conductive heat transfer mechanism is almost prevailing on the bottom. When increasing the aspect ratio, as reported in Figs 5 and 6 the recirculation expands in the whole cavity, while the buoyancy driven flow pattern and convection heat transfer increase.

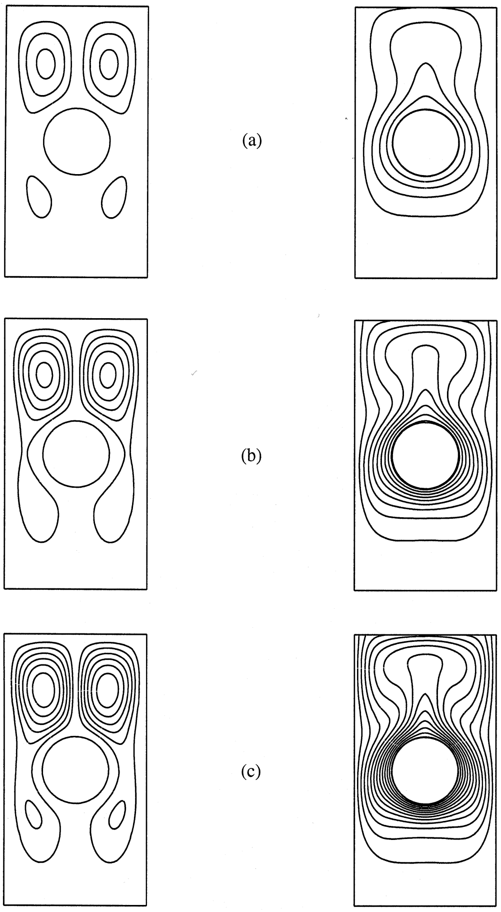

Fig. 4. Calculated streamlines (-2.5×10^{-3} (0.25×10^{-4}) 2.5×10^{-3}) and temperature (1 K) distributions in the $W^* = 2.1$ cavity: (a) $Ra = 1.3 \times 10^3$, (b) $Ra = 2.4 \times 10^3$ and (c) $Ra = 3.4 \times 10^3$.

For a qualitative comparison between the numerical and experimental temperature distributions, in Fig. 7 the calculated temperature maps are represented by means of different grey tones and compared with actual temperature distributions measured in the experimental tests.

A more exhaustive investigation of the heat transfer phenomena and a better comparison between the numerical and experimental methods can be seen from the local Nusselt number on the cylinder surface. In Figs 8–10 the Nusselt number distribution on the cylinder surface is represented for three values of the Rayleigh number investigated. Both the calculated and the experimental values are reported, and a very good agreement is reached for high values of the angle α, while a poorer agreement is found for lower values of α, with the maximum local deviation up to 22%. This is probably due to difficulties in evaluating the interferograms: the origin of the wall of the cylinder is not exactly known since the contour of the surface is blurred because of diffraction effects. The interference fringe closest to the wall is superposed on the diffraction pattern, so that its position cannot be

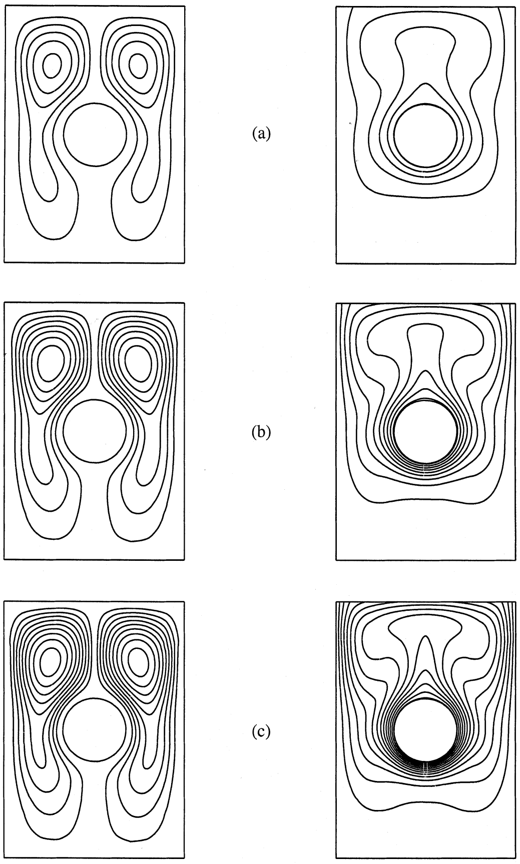

Fig. 5. Calculated streamlines (-2.5×10^{-3} (0.25×10^{-4}) 2.5×10^{-3}) and temperature (1 K) distributions in the $W^* = 2.9$ cavity: (a) $Ra = 1.3\times10^3$, (b) $Ra = 2.4\times10^3$ and (c) $Ra = 3.4\times10^3$.

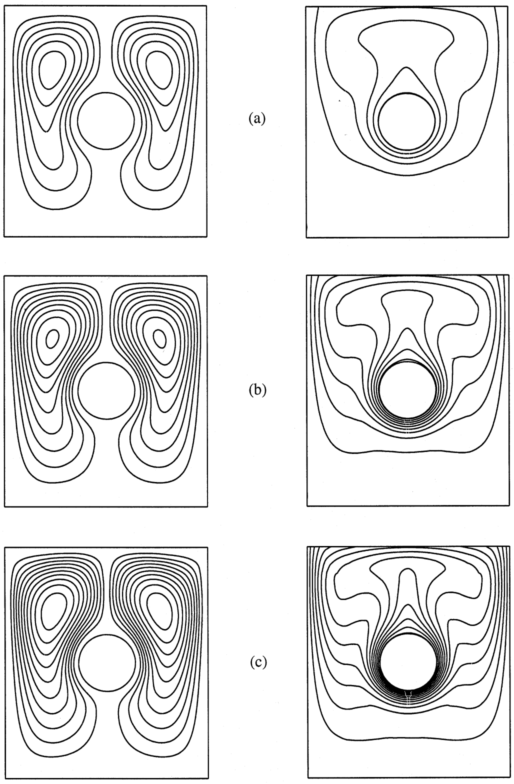

Fig. 6. Calculated streamlines (-2.5×10^{-3} (0.25×10^{-4}) 2.5×10^{-3}) and temperature (1 K) distributions in the $W^* = 3.6$ cavity: (a) $Ra = 1.3\times10^3$, (b) $Ra = 2.4\times10^3$ and (c) $Ra = 3.4\times10^3$.

precisely determined. This problem is partly overcome by extrapolating the temperature distribution derived from the interference pattern, because the temperature of the surface of the cylinder is known by means of a thermocouple measurement.

After looking at Figs 8–10, we can see how the heat transfer is strongly influenced by the Rayleigh number and the aspect ratio of the cavity. The Nusselt number distribution on the cylinder surface is characterised by an oscillating behaviour at $W^* = 2.1$ and 2.9. This confirms that the conductive heat transfer from the cylinder to the cavity is predominant in these conditions. At $W^* = 3.6$ the Nusselt number distribution is monotonically decreasing, because the convective heat transfer becomes more important.

In each of the above mentioned simulations, a numerical stationary solution is obtained, and an actual steady state regime is found experimentally. In Figs 11 and 12, frames taken from a real-time video recording are shown, to demonstrate the evolution of the temperature field during the transient regime at the beginning of the heating process, at $Ra = 2.4\times10^3$ and $Ra = 7.7\times10^3$ respectively. Before $\vartheta = 0$, both the walls and the cylinder are at uniform room temperature; at $\vartheta = 0$, the heat transfer fluids circulate into the wall jackets and into the cylinder. Due to the high flow rates utilised and to the high thermal diffusivity of the solid materials, uniform temperature distributions are reached in a few seconds. The correct temperature differences are reached in some minutes.

Additional numerical simulations were also performed for a wider cavity having $W^* = 4.3$, up to Rayleigh numbers sufficiently high to induce non-stationary and oscillating solutions. In Table 1 the calculated average Nusselt number values are reported for each geometry and several Rayleigh numbers, together with the experimental values whenever available. Non-stationary oscillating solutions are encountered at $Ra = 1.0\times10^5$ for all the W/D ratios.

The highest values of the Nusselt number calculated at the various Rayleigh numbers are marked in bold face, so that the influence of both the Rayleigh number and the aspect ratio of the cavity on the calculated Nusselt number is evident. When increasing the Rayleigh number, the highest average heat transfer coefficients are

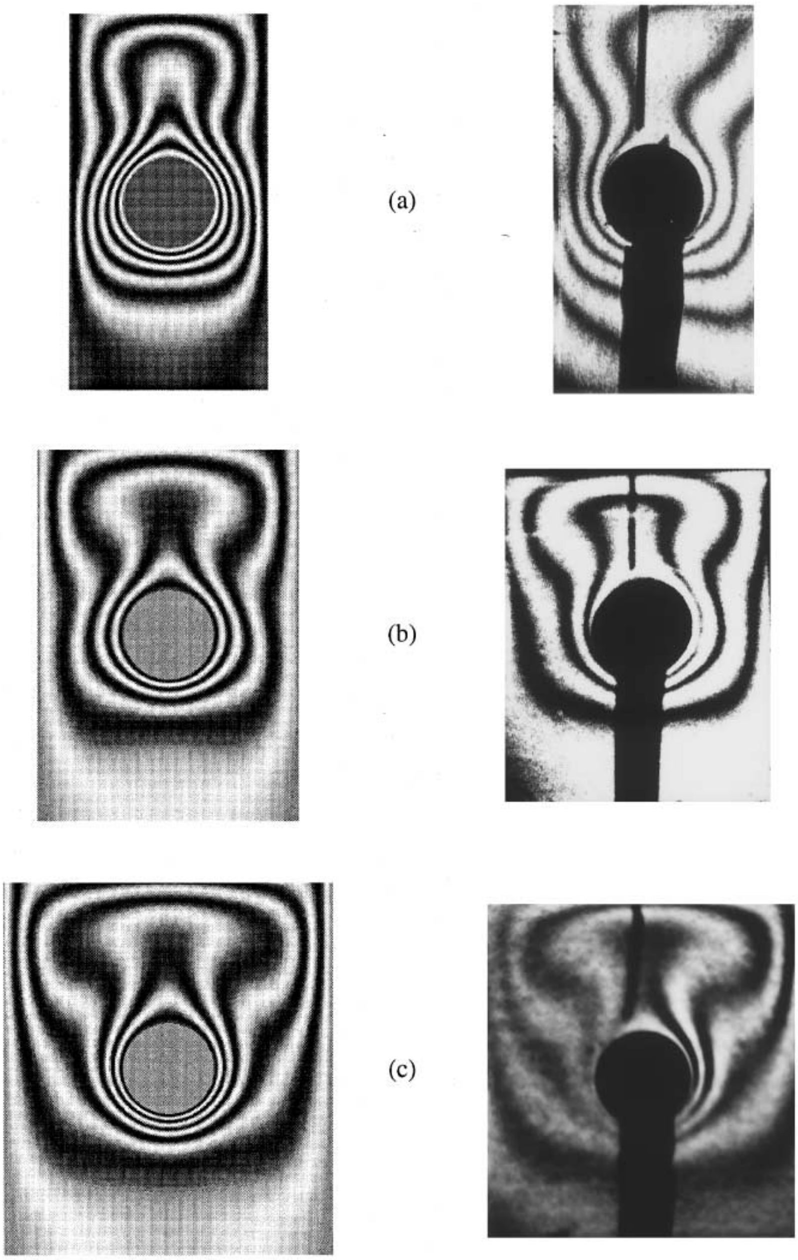

Fig. 7. Calculated temperature distributions and measured temperature distributions (interferograms) at $Ra = 1.3 \times 10^3$: (a) $W^* = 2.1$, (b) $W^* = 2.9$ and (c) $W^* = 3.6$.

encountered at decreasing aspect ratios W^*. As an example, at $Ra = 2.4 \times 10^3$ the highest Nusselt number is found at $W^* = 3.6$, while at $Ra = 7.5 \times 10^4$ the highest Nusselt number is found at $W^* = 2.1$. This is almost entirely due to the recirculation in the lower part of the cavity, which, for the narrow cavity, becomes more important at high Rayleigh numbers only. At $Ra = 1.3 \times 10^3$, the highest Nusselt number is found at $W^* = 4.3$, but another maximum is encountered at $W^* = 2.1$, due to conductive heat transfer. However, the heat transfer coefficient is mainly influenced by the Rayleigh number, and the effect of the aspect ratio of the cavity is less important.

The results reported in Table 1 are displayed graphically in Fig. 13, which shows the average Nusselt number as a function of the Rayleigh number at the various aspect ratios W^*. The diagram shows clearly the prevailing influence of the Rayleigh number.

Table 1
Average value of the Nusselt number on the cylinder surface $\overline{Nu}$

	$W^* = 2.1$		$W^* = 2.9$		$W^* = 3.6$		$W^* = 4.3$
	calc.	exp.	calc.	exp.	calc.	exp.	calc.
$Ra = 1.3 \times 10^3$	2.36	2.46	2.25	2.54	2.35	2.35	**2.38**
$Ra = 2.4 \times 10^3$	2.61	2.80	2.65	3.00	**2.75**	2.79	2.73
$Ra = 3.4 \times 10^3$	2.77	3.07	2.90	3.15	**2.98**	3.06	2.94
$Ra = 5.0 \times 10^3$	2.99	—	3.22	—	**3.25**	—	3.16
$Ra = 1.0 \times 10^4$	3.52	—	**3.80**	—	3.74	—	3.64
$Ra = 2.0 \times 10^4$	4.27	—	**4.42**	—	4.29	—	4.22
$Ra = 3.0 \times 10^4$	4.78	—	**4.80**	—	4.67	—	4.63
$Ra = 4.0 \times 10^4$	**5.17**	—	5.09	—	4.99	—	4.94
$Ra = 5.0 \times 10^4$	**5.47**	—	5.33	—	5.25	—	5.21
$Ra = 7.5 \times 10^4$	**6.05**	—	5.82	—	5.77	—	5.73

The highest calculated values at each Rayleigh number are shown in bold face

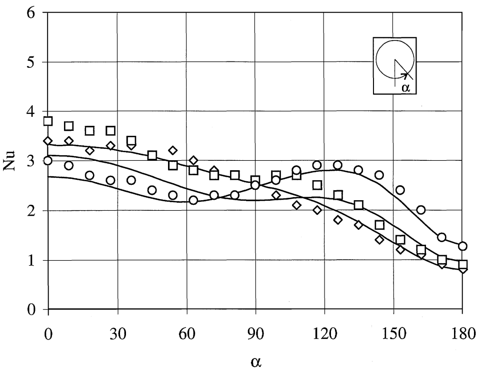

Fig. 8. Calculated and experimental local Nusselt number distribution in the cylinder surface at Ra 1.3×10^3: (○) $W^* = 2.1$, (□) $W^* = 2.9$ and (◇) $W^* = 3.6$.

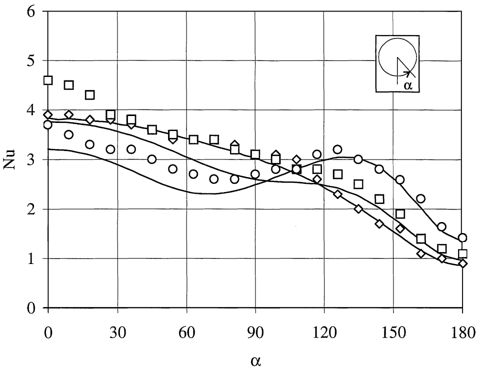

Fig. 9. Calculated and experimental local Nusselt number distribution in the cylinder surface at Ra 2.4×10^3: (○) $W^* = 2.1$, (□) $W^* = 2.9$ and (◇) $W^* = 3.6$.

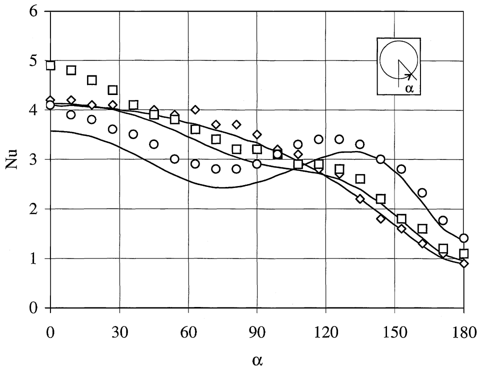

Fig. 10. Calculated and experimental local Nusselt number distribution in the cylinder surface at Ra 3.4×10^3: (○) $W^* = 2.1$, (□) $W^* = 2.9$ and (◇) $W^* = 3.6$.

5. Conclusions

The heat transfer by natural convection from a horizontal cylinder enclosed in a rectangular cavity is investigated. The numerical and experimental results are in good accordance as regards the average Nusselt number and the temperature patterns, while the experimental measurement of local Nusselt number suffers some difficulties in the evaluation of the interferograms. The influence both of the cavity aspect ratio and of the Rayleigh number on the temperature distribution and on the Nusselt number are investigated. When increasing the Rayleigh number, increasing average heat transfer coefficients are encountered, whose maximum is found at decreasing aspect ratios W^*.

At $Ra = 1 \times 10^5$ non-stationary and oscillating solutions are encountered. The investigation of the heat transfer from the cylinder to the cavity in these conditions is currently being more deeply investigated.

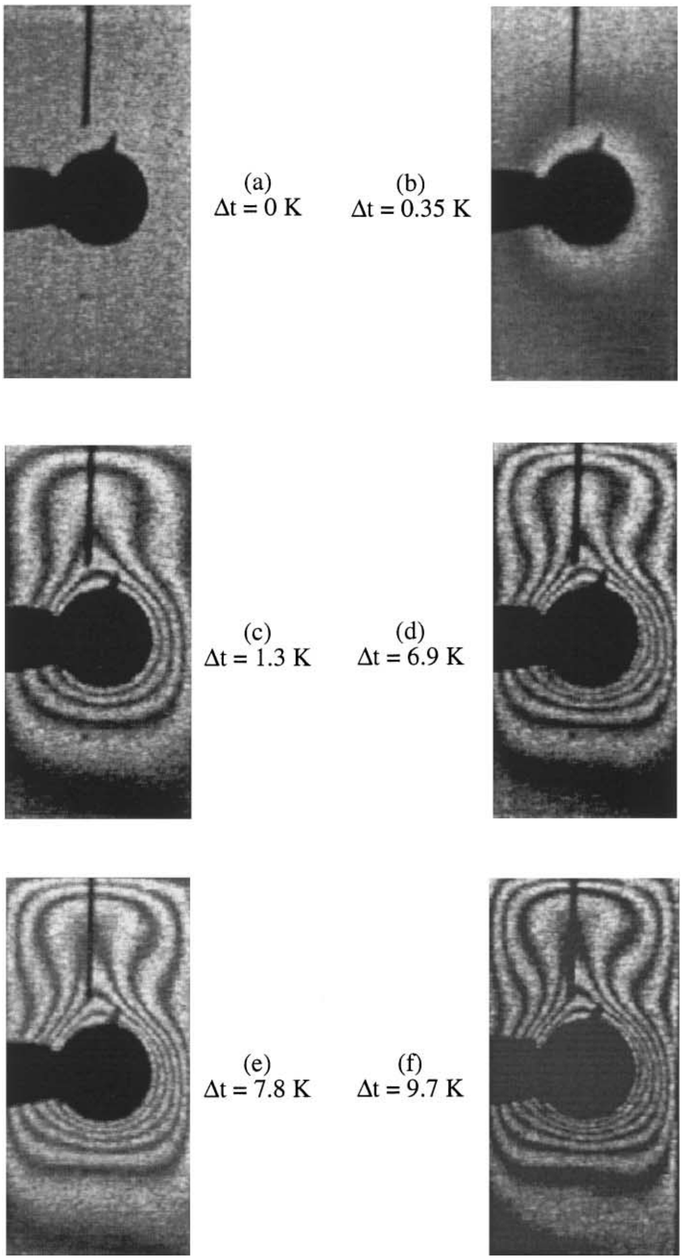

(a) $\Delta t = 0$ K

(b) $\Delta t = 0.35$ K

(c) $\Delta t = 1.3$ K

(d) $\Delta t = 6.9$ K

(e) $\Delta t = 7.8$ K

(f) $\Delta t = 9.7$ K

Fig. 11. Real time interferograms at *Ra* 2.4×10^3: (a) $\vartheta = 0$ s, (b) $\vartheta = 28$ s, (c) $\vartheta = 37$ s, (d) $\vartheta = 1111$ s. The temperature difference Δt between the average temperature of the cylinder and the average temperature of the isothermal walls is indicated.

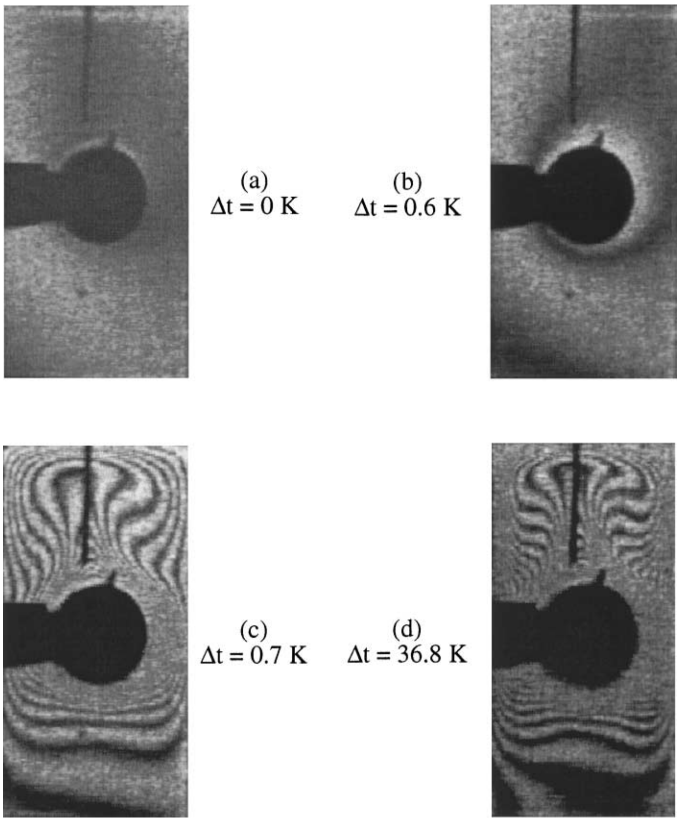

Fig. 12. Real time interferograms at Ra 7.7×10^3: (a) $\vartheta = 0$ s, (b) $\vartheta = 28.2$ s, (c) $\vartheta = 37$ s, (d) $\vartheta = 52$ s (e) $\vartheta = 61$ s, (f) $\vartheta = 671$ s. The temperature difference Δt between the average temperature of the cylinder and the average temperature of the isothermal walls is indicated.

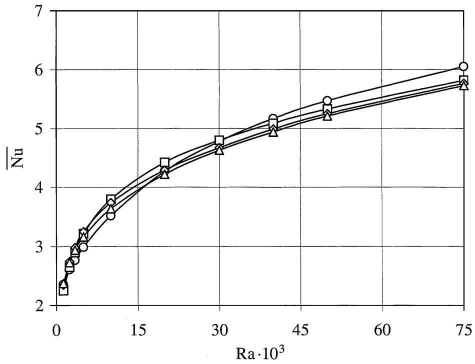

Fig. 13. Calculated average Nusselt number as a function of the Rayleigh number: (○) $W^* = 2.1$, (□) $W^* = 2.9$, (◇) $W^* = 3.6$ and (△) $W^* = 4.3$.

References

[1] B. Farouk, S.I. Güçeri, Natural convection from horizontal cylinder—laminar regime, ASME J Heat Transfer 103 (1981) 522–526.

[2] I. Tokura, H. Saito, K. Kishinami, K. Muramoto, An experimental study of free convection heat transfer from a horizontal cylinder in a vertical array set in a free space between parallel walls, ASME J. Heat Transfer 105 (1983) 102–107.

[3] V. Dakshina Murty, A numerical investigation of Benard convection using finite elements, Computers and Fluids 14 (1986) 379–391.

[4] E. Evren-Selamet, Solution of Benard problem with the projection method, Int. Comm. Heat Mass Transfer 22 (1995) 59–70.

[5] G. De Vahl Davis, Natural convection of air in a square cavity: a benchmark numerical solution, Int. J. Numer. Methods Fluids 3 (1983) 249–264.

[6] G. Comini, G. Cortella, M. Manzan, A streamfunction-vorticity based finite-element formulation for laminar-convection problems, Numer. Heat Transfer, Part B 28 (1995) 1–22.

[7] P. Le Quéré, Accurate solutions to the square thermally driven cavity at high Rayleigh number, Computers and Fluids 20 (1991) 29–41.

[8] M. Manzan, G. Cortella, G. Comini, Finite element solution of the streamfunction–vorticity equations for flow past a circular cylinder, Proceedings of the Ninth International Conference on Numerical Methods in Laminar and Turbulent Flow, vol. 9, Part II, Atlanta, 1995, pp. 1515–1526.

[9] G. Comini, M. Manzan, C. Nonino, Finite element solution of the streamfunction–vorticity equations for incompressible two-dimensional flows, Int. J. Numer. Methods Fluids 19 (1994) 513–525.

[10] G. Cesini, M. Paroncini, R. Ricci, Holographic interferometry for heat transfer studies, Proceedings of the First International Conference on New Laser Technologies and Applications, Olympia, Greece, 1988, pp. 455–468.

[11] W. Hauf, U. Grigull, Optical methods in heat transfer, Adv. in Heat Transfer 6 (1970) 133–311.